Structural characterization of fungus-specific histone deacetylase Hos3 provides insights into developing selective inhibitors with antifungal activity

Ningning Pang[1,‡] , **Jixue Sun**[1,‡], **Shiyou Che**[1,2], and **Na Yang**[1,*]

From the [1]*State Key Laboratory of Medicinal Chemical Biology, College of Pharmacy and Key Laboratory of Medical Data Analysis and Statistical Research of Tianjin, Nankai University, Tianjin, China;* [2]*College of Chemistry, Tianjin Normal University, Tianjin, China*

Edited By Brian Strahl

Fungal infection has long been a chronic and even life-threatening problem for humans. The demand for new anti-fungal drugs has increased dramatically as fungal infections have continued to increase, yet no new classes of drugs have been approved for nearly 15 years due to either high toxicity or development of drug resistance. Thus, validating new drug targets, especially fungus-specific targets, may facilitate future drug design. Here, we report the crystal structure of yeast Hos3 (*Sc*Hos3), a fungus-specific histone deacetylase (HDAC) that plays an important role in the life span of fungi. As acetylation modifications are important to many aspects of fungal infection, the species specificity of Hos3 makes it an ideal target for the development of new antifungal drugs. In this study, we show that *Sc*Hos3 forms a functional homodimer in solution, and key residues for dimerization crucial for its deacetylation activity were identified. We used molecular dynamics simulation and structural comparison with mammalian *h*HDAC6 to determine unique features of the *Sc*Hos3 catalytic core. In addition, a small-molecule inhibitor with a preference for *Sc*Hos3 was identified through structure-based virtual screening and *in vitro* enzymatic assays. The structural information and regulatory interferences of *Sc*Hos3 reported here provide new insights for the design of selective inhibitors that target fungal HDAC with high efficiency and low toxicity or that have the potential to overcome the prevailing problem of drug resistance in combination therapy with other drugs.

High mortality caused by fungal infections, especially invasive fungal infections have become a life-threatening problem (1). More than 300 million people worldwide are afflicted with serious fungal infections, and 1.5 million are in danger of losing their lives each year (2). More than 600 species of fungus are associated with human diseases (3), of which four are responsible for more than 90% of reported deaths due to fungal infection: *Cryptococcus*, *Candida*, *Pneumocystis*, and *Aspergillus* (4). In recent years, the increase in hematopoietic stem cell transplantation, the widespread use of immunotherapeutic drugs, and the use of indwelling medical devices have led to a whole new group of patients being at risk for fungal infection (5). As the number of fungi caused infections is still increasing, the demand for antifungal agents has increased dramatically.

Most antifungal drugs developed before the 1990s act by perturbing the formation of the cell membrane in fungi. These drugs can be classified into several major groups, including polyenes, second-generation azoles, allylamines, flucytosines, and echinocandins (6–11). They are effective and save lives. However, many patients with deep fungal infection, like that caused by invasive aspergillosis, still die. Furthermore, since the last echinocandin, anidulafungin, was introduced to the market in 2006, no new classes of antifungal drugs were approved, as most candidate drugs either are highly toxic (cannot be taken orally), have problems with drug resistance, or have drug interactions (12). The validation of new drug targets, especially fungus-specific targets, may provide new clues for solving this problem.

Acetylation on lysine residues of histone is a major post-translational modification (13–15). For instance, acetylation of lysine 56 of histone H3 (H3K56ac) is important for the assembly of histones into nucleosomes following DNA replication and repair (16–18). Histone acetylation levels are dynamically regulated by histone acetyltransferases (19) and histone deacetylases (HDACs) (20), and the disruption of balanced cycles of acetylation and deacetylation is associated with certain pathologies, such as neurological disease, cancer, and immunologic derangement (21, 22). Protein acetylation modification, which regulates multiple cellular processes and affects the entire cell cycle, is widely found in fungi (23–25). Studies have suggested that inhibiting fungal HDACs may have beneficial and synergistic effects, like reducing the virulence and growth of *Candida* spp. as well as decreasing their resistance to antifungal drugs (26). For example, the antifungal agent MGCD290 targeting fungal HDAC (Hos2) potentiates the activity of echinocandin against echinocandin-resistant *C.* spp. (27). Inhibition of the activity of *Aspergillus fumigatus* HDAC (RpdA) significantly delays its germination, growth, and conidiation. These findings point to HDAC inhibitors (HDACi) as a promising class of drugs for treating fungal

infections (28, 29). Moreover, developing HDACi targeting fungal-specific HDACs will lower the toxicity of these antifungal drugs.

Like mammalian HDACs, fungal HDACs are grouped into three classes: class I includes Rpd3, Hos1, Hos2, and Hos3; class II has just one member, Hda1; and the members of class III, including Sir2, Hst1, Hst2, Hst3, and Hst4, are NAD dependent (30). Of these HDACs, Hos3 exists only in fungus. It was first reported in yeast, and it plays an important role in regulating transcription silencing during the G1/S transition of the mitotic cell cycle (31, 32). Andrew *et al.* (31) found that although Hos3 can catalyze deacetylation on all four core histones (H3, H4, H2A, and H2B), it preferentially deacetylates histone H4, especially on sites lysine 5 and 8 (H4K5 and H4K8). Ahn *et al.* (33) later reported that Hos3-mediated deacetylation of H2BK11ac is related to the phosphorylation of H2BS10 and induces activation of the yeast apoptosis pathway. In addition to histone substrates, Hos3 also has nonhistone substrates. It functions as a spindle position checkpoint by latching onto spindle pole bodies to deacetylate potential substrates and inhibit mitotic exit (34). In addition, Hos3-dependent deacetylation of nuclear pore complexes directs cell cycle entry during asymmetric division of budding yeast (35). Therefore, the species specificity and biological function of Hos3 make it a promising target for antifungal drugs.

It is interesting that Hos3 is insensitive to known classic HDACi-like trichostatin A (TSA), a pan inhibitor that targets the conserved catalytic domain of mammalian HDACs (31). In addition, Hos3 functions in the form of a homodimer instead of forming complexes with other proteins like mammalian HDACs. These features make Hos3 a good target for the development of fungus-specific HDACi. However, a lack of structural information impedes the depiction of the molecular mechanism governing the specificity of Hos3 catalyzation and organization, which are important for rational drug design.

In this study, we examined the crystal structure of *Saccharomyces cerevisiae* Hos3 (*Sc*Hos3) and revealed the key residues of *Sc*Hos3 dimerization that are crucial for its deacetylation activity. Using molecular dynamics (MD) simulation and structural comparison with mammalian *h*HDAC6, we depicted specific features of the *Sc*Hos3 catalytic core. Based on these findings, we performed structure-based virtual screening to screen *Sc*Hos3-specific HDACi. Small-molecule compounds with good *in vitro* inhibition activity on fungal HDACs were found, and their selectivity against mammalian *h*HDAC6 was evaluated.

Results

The overall structure of ScHos3

We initially attempted to crystallize full-length *Sc*Hos3 (a.a. 1–697), but no crystals were observed. We used limited proteolysis to promote crystallization (36). Elastase (1:500 w/w) was added to the protein solution, and after 30 min of digestion, a stable fragment appeared on examination by SDS-PAGE (Fig. S1). Subsequent N-terminal sequencing coupled

with mass spectrometry was used to determine the N-terminal and C-terminal residues of the fragment, which were A34 and A510 (Fig. S2). By cloning the region of the gene that encodes A34 to A510, we were able to express and purify good-quality recombinant *Sc*Hos3 (a.a. 34–510) and successfully crystallize it.

The crystal structure of *Sc*Hos3 (a.a. 34–510) was determined by single wavelength anomalous dispersion at 2.4 Å resolution (PDB ID: 7WJL). All residues in the structure were well defined, except the regions encompassing residues S378-R381, Y463-D470, and D497-A510 were invisible (Fig. 1A). *Sc*Hos3 had a low sequence similarity to other mammalian HDACs. It shared ∼30% sequence identity with class I HDACs and ∼25% with class II HDACs (Fig. S3). However, the overall structure of *Sc*Hos3 was quite similar to that of previously determined class I and II HDACs, which includes a typical Rossmann fold with a central eight-stranded parallel β-sheet (β2–β9) surrounded by ten α-helices (α1–α10). Structural alignment with DALI showed that *Sc*Hos3 most resembled the CD2 domain of *h*HADC6, with a root-mean-square deviation (RMSD) of only 1.93 Å (https://www.ebi.ac.uk/msd-srv/ssm/). Besides the conserved globular rigid part, an additional β1-strand was antiparallel to the β-sheet and connected to α11 through a short loop. β1 and α11, together with α12 and the C-terminal helices (αC), formed the flexible part of the *Sc*Hos3 structure, which was different from other HDACs (Fig. 1, B and C).

The catalytic center of *Sc*Hos3 lay on the loop regions of the central αβ fold (Fig. 1A). The active site was composed of one tyrosine residue Y418 and two histidine residues H195 and H196 as well as a Zn^{2+} ion tetracoordinated by D233, H235, and D370 (Fig. 2A). Moreover, small side-chain hydrophobic residues, including G416, G417, and L234 were close to the Zn^{2+} ion binding area, and all aforementioned residues were well conserved in other HDACs (Figs. 2A and S3). Unlike other HDACs, no water molecules or K^+ ions were identified in the active center of the *Sc*Hos3 structure (37) because of either poor density mapping or the wider aperture of the outer catalytic funnel of *Sc*Hos3 compared to other HDACs that allowed free movement of small molecules in and out (Fig. 2B; see below).

The catalytic center of *Sc*Hos3 was deep into a catalytic funnel on the surface. Compared to other HDACs, the catalytic funnel of *Sc*Hos3 was wider and more negatively charged (Fig. 2B). Two α-helices, α11 and α12, as well as two loop regions, loop A and loop B, formed the outer layer of the catalytic funnel (Fig. 1B). However, these regions differed quite a bit between the structures of *h*HDAC6 and *h*HDAC1 and the *Sc*Hos3 structure, as α11 and α12 were substituted by loop regions and loop B was replaced with a helix in both the *h*HDAC6 and *h*HDAC1 structures (Fig. 1, B and C). It is worth mentioning that loop A was very flexible in the *Sc*Hos3 structure, as part of the density map of this region was invisible in the structure, whereas a similar loop at this position in *h*HDAC6 and *h*HDAC1 was shorter and better defined. These structural differences are crucial clues to designing *Sc*Hos3-specific HDACi.
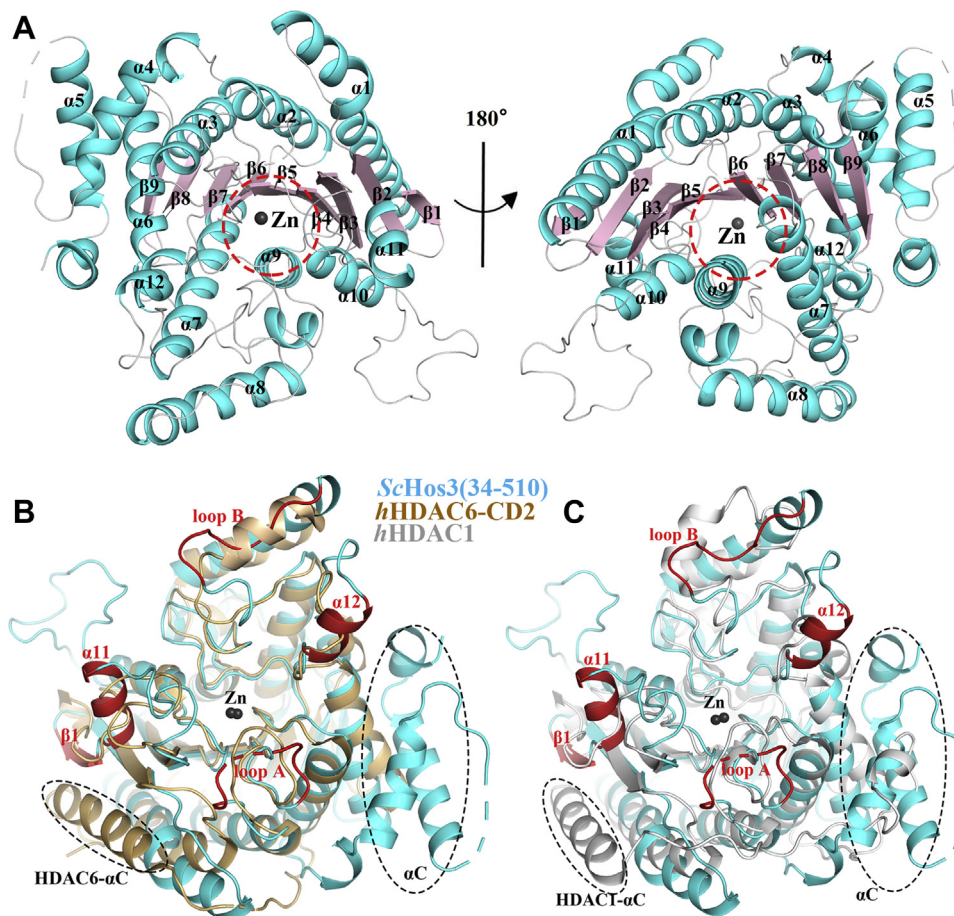
Figure 1. The overall structure of *Sc*Hos3. *A*, ribbon diagram of *Sc*Hos3 (a.a. 34–510). Helices, β-sheets, loops, and a Zn^{2+} ion are shown in *cyan*, *purple*, *gray*, and *black*, respectively. The catalytic center is *circled* in *red*. *B*, superposition of *Sc*Hos3 (*cyan*) with *h*HDAC6-CD2 (PDB ID: 5EDU; *light brown*). *C*, superposition of *Sc*Hos3 with *h*HDAC1 (PDB ID: 4BKX; *gray*). α11, α12, loop A, loop B, and β1 of *Sc*Hos3 are highlighted in *red*. Helices of the *C* terminus of *Sc*Hos3 (αC), *h*HDAC6 (HDAC6-αC), and *h*HDAC1 (HDAC1-αC) are *circled* in *black*. Hos3, HDA one similar 3; *Sc*Hos3, *Saccharomyces cerevisiae* Hos3.

The homodimer surface of *Sc*Hos3

As mentioned, *Sc*Hos3 forms a homodimer with intrinsic HDAC activity (31). To verify the dimerization state of *Sc*Hos3 in solution, we performed size-exclusion chromatography coupled to multi-angle light scattering (SEC-MALS) experiments on both full-length and crystallized *Sc*Hos3 (a.a. 34–510). The SEC-MALS results showed that the full-length *Sc*Hos3 was not stable and exhibited several states of aggregation in solution, which is a possible reason why it is unable to be crystallized from the full-length protein. By contrast, the crystallized *Sc*Hos3 was very uniform in size, with a molecular weight of ∼110 kDa, a value twice the calculated mass of monomer *Sc*Hos3 of 54 kDa (Fig. S4*A*). Moreover, *in vitro* enzymatic activity assay showed that the crystallized *Sc*Hos3 exhibited comparable deacetylation activity to the full-length *Sc*Hos3 (Fig. S4*B*). Thus, the crystallized *Sc*Hos3 (a.a. 34–510) was used for the following experiments unless explicitly specified.

As the homodimer state of *Sc*Hos3 in solution was confirmed, we set out to investigate the dimerization surface by structural analysis and site-directed mutagenesis. Although there was only one monomer in the asymmetric unit of the *Sc*Hos3 structure, a homodimer could be observed by symmetric operation in the

crystal lattice (Fig. 3*A*). Interactions between the two monomers occurred principally on the α11 helix and the subsequent β1 strand, which are unique to the *Sc*Hos3 structure. The dimerization interface buried a total surface area of ∼2330 Å², which indicates a rather strong intermolecular interaction. Polar interactions were major forces at the dimerization surface. In particular, side-chain amino group of K298 interacted with side-chain carboxyl group of E295 of the other molecule, and these two pairs of residues on the α11 helix formed the central interface of dimerization. Intermolecular polar interactions also occurred between side-chain amino group of K294 on the α11 helix and main-chain carbonyl group of K251 as well as between side-chain amino group of H308 at the end of the β1 strand and main-chain carbonyl group of I282. Furthermore, S301 and C303 on the loop region between α11 and β1 interacted with each other by main-chain carbonyl and amide groups, respectively (Fig. 3*B*).

To test whether the aforementioned residues on the interaction interface are crucial for the dimerization state of *Sc*Hos3, we designed, expressed, and purified several mutants of *Sc*Hos3. Their apparent molecular weights were examined by gel-filtration chromatography. First, we mutated both central K298 and K294 residues to alanine residues (KKmut);
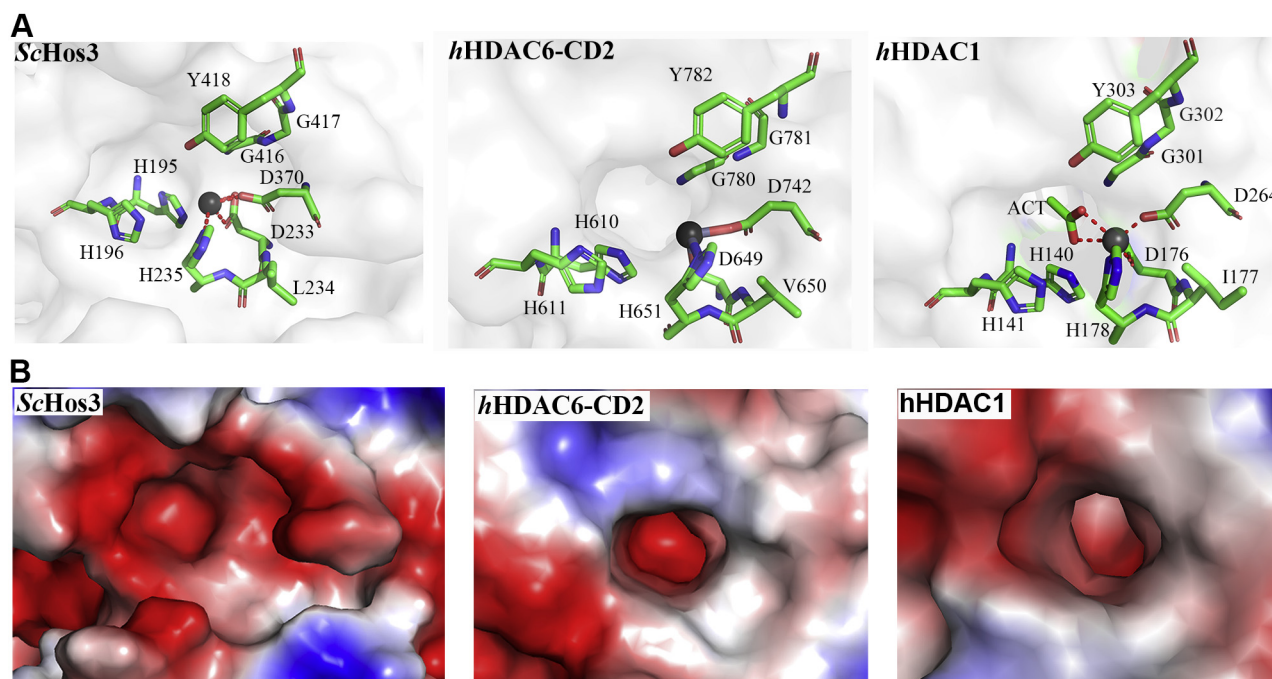
Figure 2. Comparison of the catalytic pockets of *Sc*Hos3 and other mammalian HDACs. *A*, a close-up of the catalytic center of *Sc*Hos3, *h*HDAC6-CD2, and *h*HDAC1. Active residues—including one tyrosine residue and two histidine residues, as well as a Zn^{2+} ion—are well conserved in these structures. *B*, electrostatic potential on the surface of the catalytic funnel of *Sc*Hos3, *h*HDAC6-CD2, and *h*HDAC1. The outer catalytic funnel of *Sc*Hos3 is wider and more negatively charged. HDAC, histone deacetylase; Hos3, HDA one similar 3; *Sc*Hos3, *Saccharomyces cerevisiae* Hos3.

this KKmut was eluted from a Superdex 200 Increase 10/300 column at 13.20 ml, which is similar to the WT (13.14 ml). A single mutation of H308A (Hmut) at the outermost interaction surface did not affect the elution position too much (Fig. S5*A*). However, when the H308A mutation was added to KKmut, this triple mutant (KKHmut) eluted from the same column with two peaks, an initial small peak at 13.14 ml and a later larger peak at 14.47 ml, which corresponded to the estimated molecular mass of a dimer and monomer, respectively (Fig. 3*C*). These results indicate that KKHmut primarily forms a monomer state in solution. Further SEC-MALS experimentation verified that the molecular mass of KKHmut was ~58 kDa (Fig. S5*B*), which is half the size of the WT dimer of 110 kDa (Fig. S4*A*). Thus, the dimerization state of *Sc*Hos3 was broken by mutating interacting residues on the central and outermost positions of the dimerization surface at the same time, which indicates a rather intimate interaction of the homodimer. More interesting is that the monomer fraction of KKHmut showed no detectable deacetylase activity in the *in vitro* deacetylation assay compared to the WT *Sc*Hos3 dimer (Fig. 3*D*), which proves that the dimerization state is the functional state of *Sc*Hos3 in solution, and interrupting the formation of the homodimer will badly compromise the deacetylase activity of *Sc*Hos3.

MD simulation

To further study the unique structural properties of the catalytic funnel of *Sc*Hos3, we used MD simulation to reveal the dynamic conformations and capture the stable state of *Sc*Hos3. The CD2 domain of *h*HDAC6, which *Sc*Hos3 most

resembled in the aforementioned DALI results, was used as a contrast of mammalian HDAC. Time evolutions of RMSD values showed that the structures of both *Sc*Hos3 and *h*HDAC6 were generally stable during the entire 200 ns of simulation, although a higher average RMSD was found in the *Sc*Hos3 system, which indicates local fluctuations of the *Sc*Hos3 structure (Fig. 4*A*). Per residue root-mean-square fluctuation (RMSF) analyses showed that most residues of *Sc*Hos3 had fluctuated little during the MD simulation, but a few regions were mobile and flexible, including residues 60 to 68 and 379 to 382 close to the catalytic funnel (Fig. 4, *B* and *C*). It is interesting that these two regions are located on α12 and loop A, respectively, which are unique sequential and structural elements of *Sc*Hos3 and the major components forming the outer layer of the catalytic funnel (Figs. 1*B* and S3). Structural superposition of the representative conformation after MD simulation and the initial conformation in the crystal structure showed that these two regions underwent apparent conformational changes and influenced the outer aperture of the catalytic funnel, which indicates their important role in regulating the enzymatic activity of *Sc*Hos3 (Fig. 4*C*). Furthermore, two distances depicting the outer aperture of the catalytic funnel around these two regions, denoted D1 and D2, were monitored during MD simulation (Fig. 4*D*). Time evolutions of the D1 and D2 distances of *h*HDAC6 were rather stable at 12 and 8 Å, respectively. However, both D1 and D2 of *Sc*Hos3 fluctuated more and ultimately tended to converge at ~9 and 14 Å after 150 ns of MD simulation (Fig. 4, *E* and *F*). These data prove that the outer catalytic funnels of *h*HDAC6 and *Sc*Hos3 differ in shape, with the latter being more flexible and regulatable. Based on these findings, we set out to perform
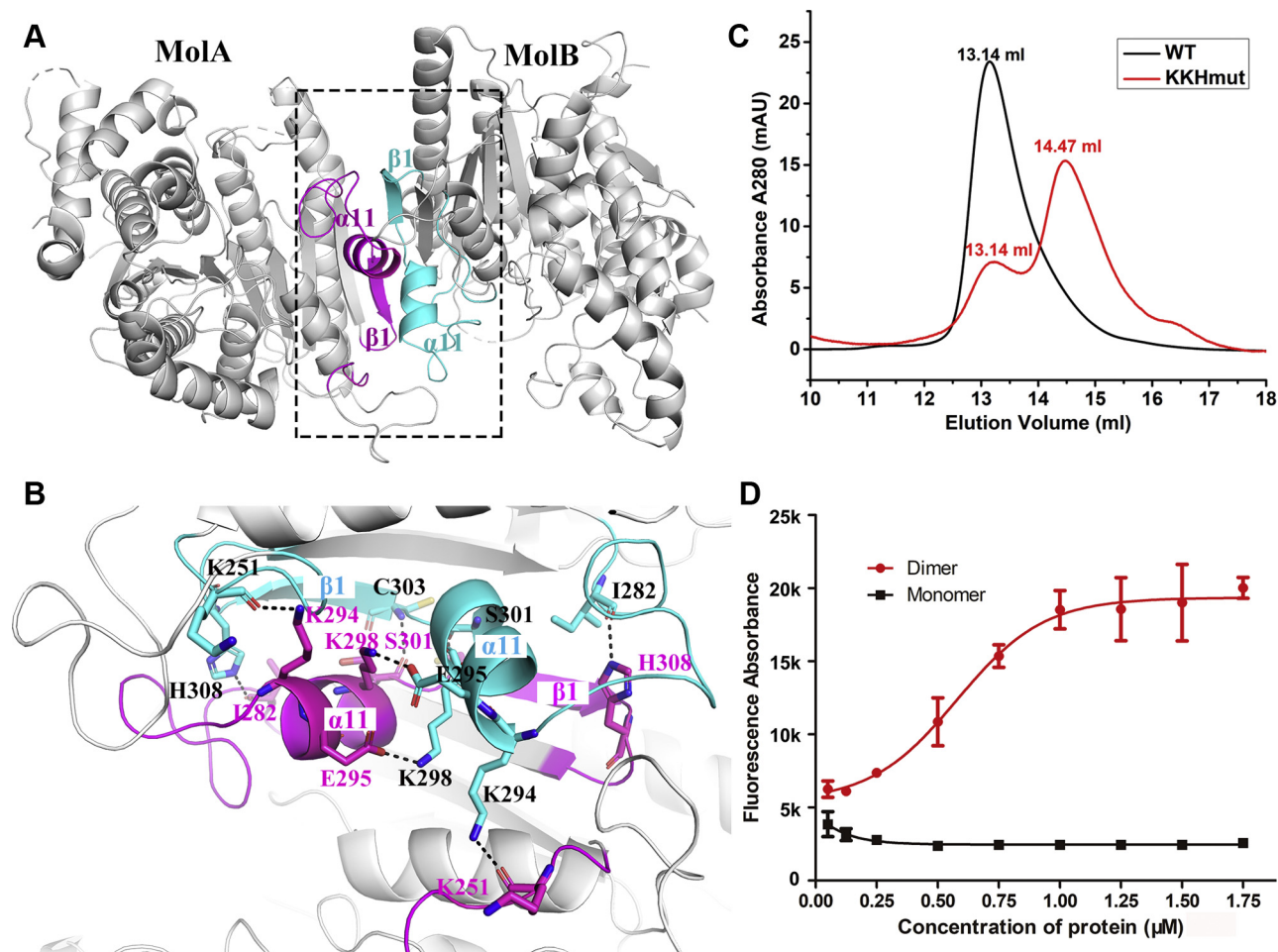
Figure 3. The dimerization state is the functional state of *Sc*Hos3 in solution. *A*, the homodimer of *Sc*Hos3 observed by symmetric operation in the crystal lattice. The dimerization interface occurs mostly on α11 and β1 of each monomer highlighted in *magenta* and *cyan*, respectively. *B*, a close-up of the dimerization interface of *Sc*Hos3. Residues involved in homodimer interactions are shown as a *stick* model. *Black dashed lines* indicate intermolecular polar interactions. *C*, comparison of the aggregation states of *Sc*Hos3 and its mutant KKHmut (K294AK298AH308A) by size-exclusion chromatography. *D*, *in vitro* deacetylation activity of the *Sc*Hos3 dimer and monomer. Hos3, HDA one similar 3; *Sc*Hos3, *Saccharomyces cerevisiae* Hos3.

structure-based virtual screening of HDACi specific for *Sc*Hos3.

HDACi specific for ScHos3

Structure-based virtual screening for small-molecule inhibitors of *Sc*Hos3 was performed as described in the Experimental Procedures section. Briefly, 13 compounds with the highest binding scores (lowest binding free energies) were selected (Table 1 and Fig. S6). *In vitro* deacetylation assay showed different inhibitory activity of these compounds against *Sc*Hos3, as their IC_{50} numbers had a wide distribution. T2383 had the lowest IC_{50} of ~0.7 μM (Fig. 5*A* and Table 1). Of note, T2383 showed a selective inhibitory effect between *Sc*Hos3 and *h*HDAC6, as the IC_{50} against *h*HDAC6 was about 4.0 μM, which is ~6 times more than the 0.7 μM of *Sc*Hos3 (Fig. 5*A*). A similar comparison was made on the reported mammalian HDACi (*R*)-TSA. The results showed that the IC_{50} of TSA against *Sc*Hos3 and *h*HADC6 were 7.5 μM and 0.2 μM, respectively (Fig. 5*A*), which proves that TSA may not be a good inhibitor of fungal HDAC (31). To check whether the

inhibitory effects of these small compounds are correlated with their binding affinities to *Sc*Hos3, we performed surface plasmon resonance (SPR) experiments and found that the dissociation constant (K_D) of T2383 bound to *Sc*Hos3 was 1.5 μM, which was much lower than that of (*R*)-TSA (42.0 μM; Fig. 5*B*) and lower than those of the other four compounds selected with inferior but tolerable inhibitory effects (Fig. S7 and Table 1). These results indicate that T2383 is a promising inhibitor specific for *Sc*Hos3.

The structural comparison showed that T2383 is Panobinostat, a pan HDACi approved by the FDA in 2015 to treat multiple myeloma (38). Like TSA and some other HDACi on the market (*e.g.*, SAHA and Belinostat), T2383 is a hydroximic acid derivative, which means it shares an identical terminal hydroximic acid group to coordinate the Zn^{2+} ion in the active center of HDACs. However, the remaining structure of T2383 was different, as it was bigger and contained more aromatic groups (Fig. S8). Further molecular docking was performed to study the structural mechanism governing the preference of T2383 bound to *Sc*Hos3. T2383 and TSA were docked into representative structures of *Sc*Hos3 and *h*HDAC6 averaged
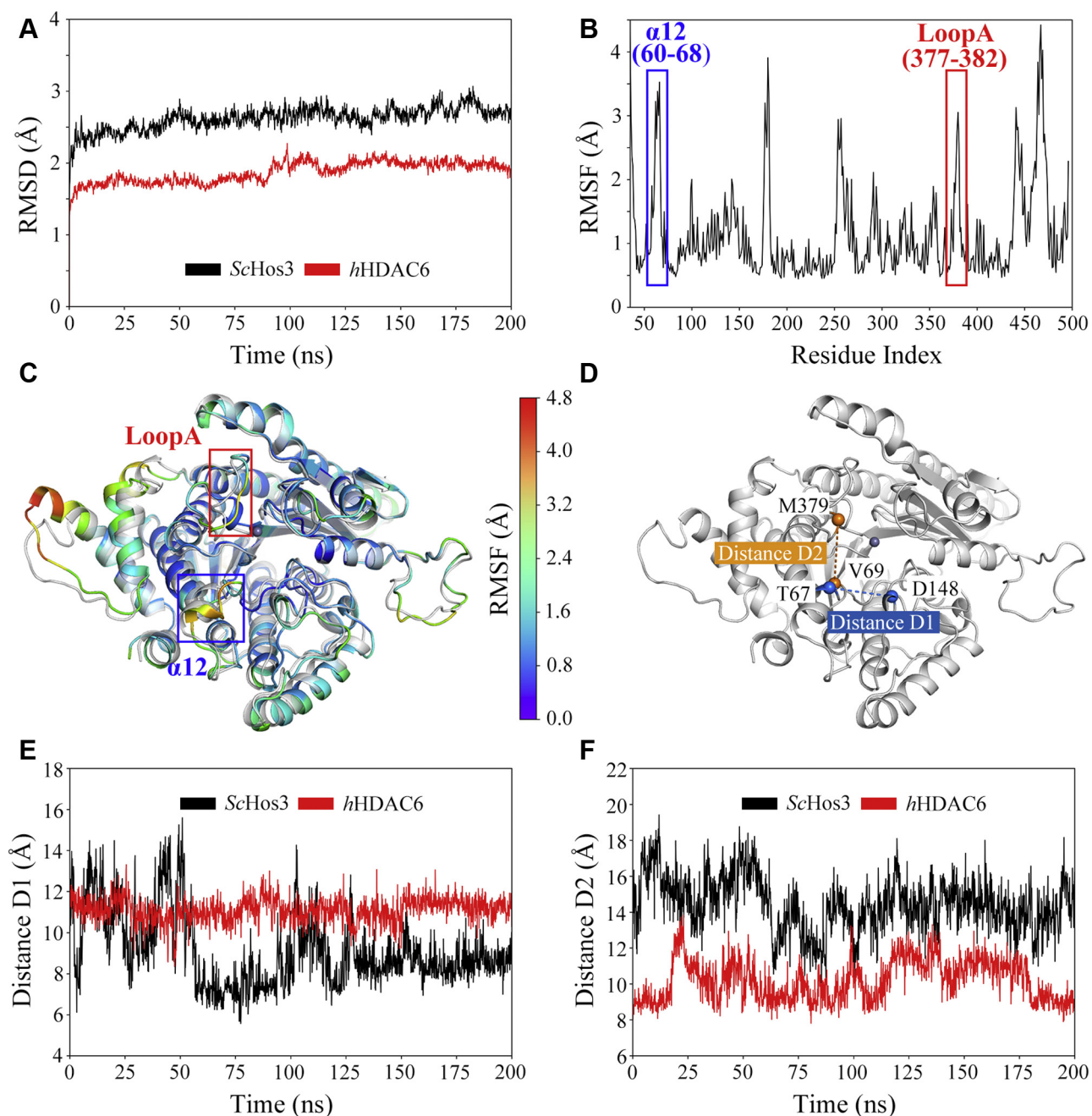
Figure 4. Structural deviation in the *Sc*Hos3 and *h*HDAC6 systems. *A*, time evolutions of RMSD values of *Sc*Hos3 and *h*HDAC6 are shown in *black* and *red*, respectively. *B*, the RMSF value of *Sc*Hos3. Residues around the catalytic funnel with large fluctuations in RMSF are marked in *red* and *blue boxes*. *C*, superpositions of representative conformation after MD simulation (colored by RMSF value) and the initial conformation in the crystal structure (*white*) of *Sc*Hos3. *D*, definition of two distances depicting the outer aperture of the catalytic funnel of *Sc*Hos3. D1: The distance between Cα atoms of residues T67 and D148; D2: The distance between Cα atoms of residues V69 and M379. *E*, time evolutions of distance D1 in *Sc*Hos3 and *h*HDAC6 structures. *F*, time evolutions of distance D2 in *Sc*Hos3 and *h*HDAC6 structures. Hos3, HDA one similar 3; MD simulation, molecular dynamics simulation; RMSD, root-mean-square deviation; RMSF, per residue root-mean-square fluctuation; *Sc*Hos3, *Saccharomyces cerevisiae* Hos3; TSA, trichostatin A.

from the last 20 ns of the MD simulation, respectively. As shown in Fig. S8, *A* and *B*, T2383 was docked into the catalytic centers of both *Sc*Hos3 and *h*HDAC6 and was close enough to coordinate the crucial Zn^{2+} ion. However, T2383 had more interactions with the surrounding residues of *Sc*Hos3, including polar interactions with the side chains of D148 and the catalytic residue Y418; π-π interactions between its phenyl group and the aromatic side chains of F205 and F285; and hydrophobic interactions between its 2-methyl indole group

and the surrounding residues T67, V69, F205, M379, and Y418 (Fig. S8*A*). By contrast, although the phenyl ring of T2383 had similar π-π interactions with F620 and F680 of *h*HADC6, the hydrophobic indole ring seemed to be isolated from the catalytic center and exposed in the solvent, which suggests a loose binding mode (Fig. S8*B*). These results were consistent with the binding free energies of T2383 to *Sc*Hos3 and *h*HADC6, which are −9.69 and −8.04 kcal/mol, respectively. Similar comparisons of the less preferential binding of (*R*)-TSA to

Table 1
Inhibitory effects and binding abilities of selected compounds to *Sc*Hos3

Number	Compound	Binding free energy (kcal/mol)	IC$_{50}$ (µM)	K$_D$ (µM)
Control	(*R*)-TSA	−7.01	7.5	42.0
1	T2383 (Panobinostat)	−9.69	0.7	1.5
2	T1890 (Pracinostat)	−8.30	4.0	9.7
3	T3509	−7.28	4.0	10.3
4	T6392	−8.71	4.3	42.8
5	T1852 (Belinostat)	−7.66	12.0	32.5
6	T6325	−7.45	35.0	-
7	K783-3813	−8.99	40.0	-
8	K783-3737	−9.13	60.0	-
9	T4370	−7.97	80.0	-
10	K783-4084	−9.03	>100	-
11	T2023	−7.27	No inhibitory activity	-
12	6049-0130	−8.57	No inhibitory activity	-
13	6049-0096	−8.33	No inhibitory activity	-

*Sc*Hos3 are shown in Fig. S8C. Polar interactions only occurred with the catalytic residue Y418, and although, like in T2383, the terminal group of TSA bent and inserted into a hydrophobic pocket formed by T67, V69, and M379, the dimethylaniline group of TSA did not seem to be as suitable for a pocket as the indole group of T2383. By contrast, (*R*)-TSA bound to *h*HADC6 in a more comfortable way (the docked conformation resembled that in the reported crystal structure of 5EDU); its hydroximic acid group formed more polar interactions with the catalytic residues Y782, H610, and H611; and the methyl group retained hydrophobic interactions with F620 and F680 (Fig. S8D). The binding free energies of TSA to *Sc*Hos3 and *h*HACD6 are −7.01 and −8.99 kcal/mol, respectively, which are consistent with the structural analyses.

As discussed previously, the α12 (a.a. 60–68) and loop A (a.a. 379–382) regions exhibited distinct sequential and structural features of the catalytic funnel of *Sc*Hos3, and two distances, D1 and D2, were defined to describe the flexibility of the outer catalytic funnel (Fig. 4). From the above docking results, we can see that the relatively larger D1 and smaller D2 of *Sc*Hos3 may promote the bending of the inhibitors and allow the free-floating terminus of the inhibitors to be stabilized in a hydrophobic pocket formed by residues mainly on α12 (T67, V69) and loop A (M379; Fig. S8, A and C). This bending may be either helpful (in the case of T2383) or harmful (TSA) to their inhibitory effects. To verify whether the hypothesized sequence differences between *Sc*Hos3 and human HDAC are indeed responsible for the preferential
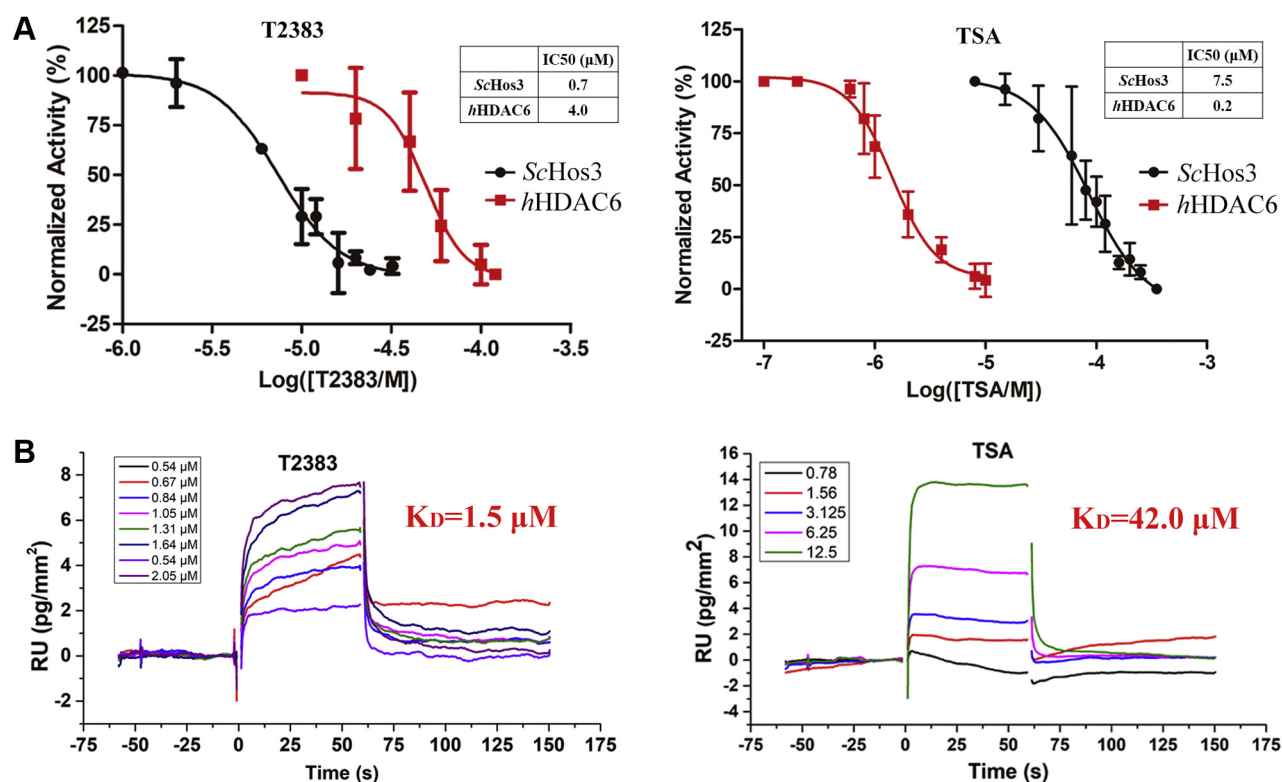

Figure 5. T2383 shows a selective inhibitory effect between *Sc*Hos3 and *h*HDAC6. *A*, inhibitory effects of T2383 (*left*) and TSA (*right*) on *Sc*Hos3 (*black curve*) and *h*HDAC6 (*red curve*). *B*, binding curves of *Sc*Hos3 to T2383 and TSA measured using SPR. The dissociation constant (*K$_D$*) is in *red*. Hos3, HDA one similar 3; *Sc*Hos3, *Saccharomyces cerevisiae* Hos3; TSA, trichostatin A.

inhibition of T2383 of *Sc*Hos3, two *Sc*Hos3 mutants with deletion of α12 (Δ62–67) or loop A (Δ379–382) were expressed, purified, and examined by *in vitro* deacetylase activity assays. Results showed the deletion of α12 (Δ62–67) badly compromised the expression level and deacetylase activity of *Sc*Hos3. By contrast, although the deletion of loop A (Δ379–382) retained the good properties of protein, T2383 had evident reduced inhibitory effect on the Δ379–382 mutant, with an IC50 of ~80 μM, compared to the 0.7 μM for WT *Sc*Hos3 (Fig. S9). These sequential and structural features of *Sc*Hos3 should be considered in the future when designing more suitable inhibitors specific for fungal HDACs.

Discussion

In this study, we elucidated the crystal structure of *Sc*Hos3, a fungus-specific HDAC that shows intrinsic HDAC activity in its dimerization form. Through MD simulation and structural comparison with its mammalian homolog *h*HADC6, we revealed the unique structural features of the catalytic funnel of *Sc*Hos3. The small-molecule inhibitor T2383 with a preference for *Sc*Hos3 was further identified through structure-based virtual screening and *in vitro* enzymatic assay. T2383, an HDACi with broad-spectrum inhibitory effects on mammalian HDACs, has been approved by the FDA to treat multiple myeloma. In our study, T2383 had a greater inhibitory effect on *Sc*Hos3 than it did on *h*HADC6 (Fig. 5A). Whether T2383 inhibits Hos3 from other fungal species, especially those with high pathogenic properties, like *Candida and Aspergillus* spp., is worthy of in-depth study. The results of sequence alignment showed that all representative fungal Hos3 (including Hos3 from yeast and other infectious species) shared common features of α12 and loop A, which are not conserved in human HDACs (Fig. S3). This indicates that T2383 can potentially inhibit other fungal HDACs that are more disease relevant. In addition, preliminary *in vitro* deacetylase activity assay showed that T2383 had a comparable inhibitory effect on *C.* spp. *Ca*Hos3, with an IC$_{50}$ of ~2.8 μM compared to 0.7 μM for *Sc*Hos3 (Fig. S10). As acetylation modifications play important roles in regulating the stress response, antifungal tolerance, and virulence of *C.* spp., *Ca*Hos3 may be a good target for the development of antifungal drugs to fight against the drug resistance and drug toxicity that are common when treating *Candida* infection. However, much work will be required to optimize T2383 from an *in vitro* inhibitory study to a finished antifungal drug. One problem is that it is usually difficult for drugs that act on cellular targets—like *Ca*Hos2 inhibitors—to penetrate the fungal membrane (39). Future reports on the co-crystal structure of *Ca*Hos3 in complex with T2383 or its analogs, followed by iterative structure–activity relationship analyses, will indeed facilitate progress.

The aforementioned studies of Hos3 inhibitors focus on the interference of its catalytic center. Intervention of the dimerization surface may also effectively hinder its activity, as the homodimer state is the functional quaternary structure of *Sc*Hos3 (Fig. 3), and *Ca*Hos3 is mostly in the

homodimer state during the purification as well. However, the dimerization surface of *Sc*Hos3 is large and cannot be easily broken by a single mutation of the interacting residue. Thus, peptide mimics like in the protein–protein interaction library may be a good choice for initial screening for interrupters of dimerization.

In summary, Hos3 is an ideal target for the development of antifungal drugs with low toxicity, as it exists only in fungi and plays an important role in their life span. The structural information about *Sc*Hos3 reported here provides new insight into the design of selective inhibitors that target fungal HDAC. It may facilitate the development of new antifungal drugs with high efficiency and low toxicity or even overcome the prevailing problem of drug resistance in combination therapy with other drugs.

Experimental procedures

Protein expression and purification

The full-length *Sc*Hos3 (a.a. 1–697) gene was amplified by PCR from the yeast genomic DNA library. Genes encoding *Sc*Hos3 and its truncation (a.a. 34–510) or mutants (H308A, K294AK298A, K294AK298AH308A) were subcloned into an engineered pET28a-smt3 vector with an N-terminal His$_6$-SUMO tag. The fusion protein was expressed in the BL21(DE3) codon plus RIL strain of *Escherichia coli*. Cells were induced by 0.2 mM isopropyl β-D-1-thiogalactopyranoside when the cell density reached A$_{600}$ ~0.8, and cell cultures were grown for an additional 20 h at 16 °C. Cells were harvested by centrifugation and resuspended in lysis buffer (20 mM Tris 8.0, 500 mM NaCl, 10 mM imidazole, 1 mM β-Me, 5 mM PMSF), then lysed by sonication. The cell lysate was clarified by centrifugation at 18,000 rpm for 50 min at 4 °C, and the supernatant was loaded onto a Ni-excel affinity column (GE healthcare). After being washed with ten column volumes of washing buffer (20 mM Tris 8.0, 500 mM NaCl, 20 mM imidazole, 1 mM β-Me), the fusion protein was eluted from the affinity column with elution buffer (20 mM Tris 8.0, 500 mM NaCl, 250 mM imidazole, 1 mM β-Me) and digested by sumo protease for 2 h at 4 °C. The sample was dialyzed to buffer A (20 mM Tris 8.0, 200 mM NaCl, 1 mM DTT) and loaded onto a HiTrap SP HP column (GE Healthcare). Untagged proteins were eluted with buffer B (20 mM Tris 8.0, 1 M NaCl, 1 mM DTT) and further purified through a HiLoad 10/300 Superdex 200 column (GE Healthcare) in buffer A. The Δ62–67 and Δ379–382 mutants of *Sc*Hos3 (a.a. 34–510) were expressed and purified as above except that the SP column purification was saved as the expression levels were low. High purified proteins were collected and concentrated for crystallization and enzymatic assays.

The gene encoding the CD2 domain of human HDAC6 (a.a. 495–850) was cloned into a pMAT9s vector in frame with an N-terminal maltose binding protein (MBP) tag. The fusion protein was expressed in the BL21(DE3) strain of *E. coli*, and cells were harvested and lysed as described above except that the lysis buffer used for the MBP affinity column was 20 mM Tris 8.0, 500 mM NaCl, and 5 mM PMSF. After being washed

with ten column volumes of washing buffer (20 mM Tris 8.0, 500 mM NaCl), the fusion protein was eluted from the affinity column with elution buffer (20 mM Tris 8.0, 500 mM NaCl, 10 mM maltose) and concentrated for enzymatic assay.

The full-length *Ca*Hos3 (a.a. 1–713) gene was cloned, expressed, and purified like the full-length *Sc*Hos3 except that a HiTrap Heparin HP column (GE Healthcare) was used instead of the SP column for ion-exchange purification. There were three peaks on the last gel-filtration chromatography. The main peak, representing a homodimer state, was collected and concentrated for enzymatic assay.

Crystallization and diffraction

All crystallization experiments were conducted at 20 °C with the sitting drop vapor diffusion method. Briefly, 1 µl *Sc*Hos3 (a.a. 34–510, ~8 mg/ml) was mixed with 1 µl reservoir solution in 48-well Cryschem plates and equilibrated against 100 µl reservoir solution. The optimized crystallization condition was 0.05 M Hepes 7.0, 0.1 M ammonium acetate, 0.02 M magnesium chloride, and 8% PEG 8000. *Sc*Hos3 crystals reached sizes suitable for X-ray diffraction after 2 to 3 days. For X-ray diffraction, the crystals were rapidly frozen in liquid nitrogen with a cryoprotectant prepared by adding 20% (v/v) glycerol to the reservoir solution. For phasing, heavy atom iodide was introduced into the crystals by soaking the crystals for 0.5 to 24 h in cryoprotectant with different concentrations of sodium iodide. All diffraction data were collected at Shanghai Synchrotron Radiation Facility Beamline BL17U using a Quantum 315r CCD detector (ADSC) at a wavelength of 0.9789 Å for native crystals and 0.9792 Å for heavy atom–soaked crystals. The diffraction images were processed with HKL2000 ([40](#)).

Determination and refinement of the crystal structure

We determined the crystal structure of *Sc*Hos3 (a.a. 34–510) using single wavelength anomalous dispersion in PHENIX ([41](#)). Prior to being used for structure refinement, 5% of reflections were randomly selected and set aside for calculating R_{free} as a monitor of model quality. Manual refinement was performed with Coot ([42](#)), and subsequent computational refinements with local noncrystallographic symmetry restraints were performed with PHENIX. Detailed statistics on data collection and refinement are summarized in Table S1. All figures of protein structures were prepared in PyMOL (http://pymol.sourceforge.net/).

Enzymatic activity assay

Deacetylation assay was performed in triplicate at 37 °C in a flat-bottom 96-well black plate (Costa). Briefly, enzymes and different concentrations of inhibitors were mixed in HDAC assay buffer (50 mM Tris 8.0, 137 mM NaCl, 2.7 mM KCl, 1.0 mM $MgCl_2$). To initiate the reaction, we added 80 µM fluorogenic substrate H4K5(Ac) peptide (GRGK[Ac]-AMC) to the aforementioned solution in a 100 µl reaction system. After incubating for 30 min, the reaction was stopped with the addition of 10 µl developer solution (1 µM trypsin and 10 µM

TSA in HDAC assay buffer). The fluorescence intensity was measured with a Tecan Spark reader (λ_{ex} = 360 nm, λ_{em} = 450 nm). To calculate IC_{50} values, we analyzed the data using logistic regression. The fluorescence intensity of the negative control (which contained 2% DMSO instead of inhibitors) was set as 100% enzymatic activity.

Size-exclusion chromatography coupled to multi-angle light scattering

SEC-MALS was used to determine the molecular weight of WT and mutant *Sc*Hos3 (a.a. 34–510) in solution. Experiments were performed at 4 °C in a buffer containing 20 mM Tris 8.0 and 200 mM NaCl. Purified protein samples (1 mg/ml, 500 µl) were injected into a Superdex 200 increase 10/300 column (GE Healthcare) and flowed through the column at a rate of 0.4 ml/min. Light scattering at 663 nm, ultraviolet absorbance at 280 nm, and the refractive index were monitored during the procedure. BSA was used to standardize the system. ASTRA 6.1 was used to record and process data.

Surface plasmon resonance

SPR experiments were performed on a BIAcore T200 SPR system (BIAcore, Cytiva) at 25 °C in Hepes buffer (20 mM Hepes 7.4, 200 mM NaCl, 5% DMSO). Protein was immobilized on CM5 chips by amine coupling, and the diluted inhibitors (0–200 µM) were flowed through the chips at a rate of 30 µl/min with solvent correction performed at the same time. Background binding to blank immobilized flow cells was subtracted, and K_D values were calculated with the 1:1 binding kinetics model or steady state affinity model built into BIAcore T200 Evaluation Software (version 3.2).

MD simulations

Two systems, hereafter designated *Sc*Hos3 and *h*HDAC6, were built to perform MD simulation. The initial structure of the two systems was derived from the crystal structure of *Sc*Hos3 determined in this work and the CD2 domain of the crystal structure of *h*HDAC6 (deduced from PDB ID: 5EDU by the removal of the MBP tag and TSA) ([43](#)), respectively. For each complex, missing residues and hydrogen atoms were added by SWISS-MODEL ([44](#)). The protonation states of histidine residues were assigned as predicted by H++ ([45](#)). The zinc ions in the crystal structure were reserved and coordinated with histidine and aspartic acid residues. The amber FF14SB force fields were used for protein ([46](#)). A TIP3P water model was used to solvate the complex in a hexagonal explicit water box under the periodic boundary condition ([47](#)). The distance between the edges of the box and the closest atoms of the complex was 12 Å. Na^+ was added as counterions to neutralize each system.

For each solvated system, 5000-step energy minimization for the whole residues was performed, followed by a combined equilibration process with a 500 ps constant volume ensemble to heat the system from 0 to 300 K and a 500 ps constant pressure ensemble at a constant pressure of 1 bar. During equilibration, a force constant of 10 kcal mol^{-1} $Å^{-2}$ as a

harmonic constraint was applied. Then 200 ns MD simulation of each system was performed with the AMBER18 software package in constant pressure ensembles at 300 K with the constraint released (48). The time step was set to 2 fs. The SHAKE algorithm was used to restrain all bond lengths involving hydrogen atoms (49). The particle mesh Ewald method was used to calculate the long-range electrostatic contributions (50). The cut-off value of the van der Waals interactions was set to 10 Å.

The cpptraj module in AmberTools18 was used to calculate the conformational descriptors along each MD simulation, including RMSDs, RMSFs, and the defined distances D1 and D2. Distance D1 was measured between the Cα atoms of residues T67 and D148 of *Sc*Hos3 and those of H500 and S568 of *h*HDAC6, respectively. Distance D2 was measured between the Cα atoms of V69 and M379 of *Sc*Hos3 and those of P501 and L749 of *h*HDAC6, respectively. The illustrated representative structure for each system was derived from the average structure during the last 20 ns of MD simulation.

Virtual screening and molecular docking

Receptor-based virtual screening was performed with the AutoDock4.2 program to screen the lead compounds against *Sc*Hos3 (51). The ligand for molecular docking was derived from an in-house virtual database that included approximately 2000 molecules and was prepared by retaining the molecules with hydroximic acid groups in the ZINC library (52). The receptor was the representative structure of *Sc*Hos3 obtained from the MD simulation. The energy grid was generated to cover the binding pocket of *Sc*Hos3 with a size of $18 \times 18 \times 18$ $Å^3$. The number of docking runs for each compound was set to 500. From both docking scoring and visual inspection, 13 compounds were selected and purchased from TopScience and examined by *in vitro* enzymatic activity assay.

In addition, molecular docking was also performed to investigate the selectivity of small-molecule inhibitors against *Sc*Hos3 and *h*HDAC6. Each receptor structure was derived from its representative structure during MD simulation. The parameters in the calculations for both systems were the same as those used in the virtual screening.

Data availability

Atomic coordinates and associated structure factors have been deposited in the Protein Data Bank (PDB ID code: 7WJL).

References

1. Hof, H. (2010) IFI = invasive fungal infections. What is that? A misnomer, because a non-invasive fungal infection does not exist! *Int. J. Infect. Dis.* **14**, e458–e459
2. Denning, D. W., and Bromley, M. J. (2015) Infectious disease. How to bolster the antifungal pipeline. *Science* **347**, 1414–1416
3. Vallières, C., Singh, N., Alexander, C., and Avery, S. V. (2020) Repurposing nonantifungal approved drugs for synergistic targeting of fungal pathogens. *ACS Infect. Dis.* **6**, 2950–2958
4. Brown, G. D., Denning, D. W., Gow, N. A., Levitz, S. M., Netea, M. G., and White, T. C. (2012) Hidden killers: human fungal infections. *Sci. Transl. Med.* **4**, 165rv113
5. Bailey, C., and Mansfield, K. (2010) Emerging and reemerging infectious diseases of nonhuman primates in the laboratory setting. *Vet. Pathol.* **47**, 462–481
6. Andes, D., and van Ogtrop, M. (2000) *In vivo* characterization of the pharmacodynamics of flucytosine in a neutropenic murine disseminated candidiasis model. *Antimicrob. Agents Chemother.* **44**, 938–942
7. Ganzinger, U., Stutz, A., Petranyi, G., and Stephen, A. (1986) Allylamines: topical and oral treatment of dermatomycoses with a new class of antifungal agents. *Acta Derm. Venereol. Suppl. (Stockh.)* **121**, 155–160
8. Kale, P., and Johnson, L. B. (2005) Second-generation azole antifungal agents. *Drugs Today (Barc.)* **41**, 91–105
9. Hamill, R. J. (2013) Amphotericin B formulations: a comparative review of efficacy and toxicity. *Drugs* **73**, 919–934
10. Kathiravan, M. K., Salake, A. B., Chothe, A. S., Dudhe, P. B., Watode, R. P., Mukta, M. S., *et al.* (2012) The biology and chemistry of antifungal agents: a review. *Bioorg. Med. Chem.* **20**, 5678–5698
11. Beyda, N. D., Lewis, R. E., and Garey, K. W. (2012) Echinocandin resistance in Candida species: mechanisms of reduced susceptibility and therapeutic approaches. *Ann. Pharmacother.* **46**, 1086–1096
12. Patil, A., and Majumdar, S. (2017) Echinocandins in antifungal pharmacotherapy. *J. Pharm. Pharmacol.* **69**, 1635–1660
13. Marmorstein, R., and Zhou, M. M. (2014) Writers and readers of histone acetylation: structure, mechanism, and inhibition. *Cold Spring Harb. Perspect. Biol.* **6**, a018762
14. Shen, Y., Wei, W., and Zhou, D. X. (2015) Histone acetylation enzymes coordinate metabolism and gene expression. *Trends Plant Sci.* **20**, 614–621
15. Shahbazian, M. D., and Grunstein, M. (2007) Functions of site-specific histone acetylation and deacetylation. *Annu. Rev. Biochem.* **76**, 75–100
16. Zhang, L., Serra-Cardona, A., Zhou, H., Wang, M., Yang, N., Zhang, Z., *et al.* (2018) Multisite substrate recognition in Asf1-dependent acetylation of histone H3 K56 by Rtt109. *Cell* **174**, 818–830.e11

17. Chen, C. C., Carson, J. J., Feser, J., Tamburini, B., Zabaronick, S., Linger, J., *et al.* (2008) Acetylated lysine 56 on histone H3 drives chromatin assembly after repair and signals for the completion of repair. *Cell* **134**, 231–243

18. Li, Q., Zhou, H., Wurtele, H., Davies, B., Horazdovsky, B., Verreault, A., *et al.* (2008) Acetylation of histone H3 lysine 56 regulates replication-coupled nucleosome assembly. *Cell* **134**, 244–255

19. Marmorstein, R., and Roth, S. Y. (2001) Histone acetyltransferases: function, structure, and catalysis. *Curr. Opin. Genet. Dev.* **11**, 155–161

20. Yang, X. J., and Seto, E. (2008) The Rpd3/Hda1 family of lysine deacetylases: From bacteria and yeast to mice and men. *Nat. Rev. Mol. Cell Biol.* **9**, 206–218

21. Falkenberg, K. J., and Johnstone, R. W. (2014) Histone deacetylases and their inhibitors in cancer, neurological diseases and immune disorders. *Nat. Rev. Drug Discov.* **13**, 673–691

22. Yoo, J., Jeon, Y. H., Lee, D. H., Kim, G. W., Lee, S. W., Kim, S. Y., *et al.* (2021) HDAC6-selective inhibitors enhance anticancer effects of paclitaxel in ovarian cancer cells. *Oncol. Lett.* **21**, 201

23. Zhou, X., Qian, G., Yi, X., Li, X., and Liu, W. (2016) Systematic analysis of the lysine acetylome in Candida albicans. *J. Proteome Res.* **15**, 2525–2536

24. Kim, J., Lee, J. E., and Lee, J. S. (2015) Histone deacetylase-mediated morphological transition in Candida albicans. *J. Microbiol.* **53**, 805–811

25. Narita, T., Weinert, B. T., and Choudhary, C. (2019) Functions and mechanisms of non-histone protein acetylation. *Nat. Rev. Mol. Cell Biol.* **20**, 156–174

26. Rajasekharan, S. K., Ramesh, S., and Bakkiyaraj, D. (2015) Synergy of flavonoids with HDAC inhibitor: new approach to target Candida tropicalis biofilms. *J. Chemother.* **27**, 246–249

27. Pfaller, M. A., Rhomberg, P. R., Messer, S. A., and Castanheira, M. (2015) *In vitro* activity of a Hos2 deacetylase inhibitor, MGCD290, in combination with echinocandins against echinocandin-resistant Candida species. *Diagn. Microbiol. Infect. Dis.* **81**, 259–263

28. Bauer, I., Varadarajan, D., Pidroni, A., Gross, S., Vergeiner, S., Faber, B., *et al.* (2016) A class 1 histone deacetylase with potential as an antifungal target. *mBio* **7**, e00831-16

29. Lamoth, F., Juvvadi, P. R., and Steinbach, W. J. (2015) Histone deacetylase inhibition as an alternative strategy against invasive aspergillosis. *Front. Microbiol.* **6**, 96

30. Ekwall, K. (2005) Genome-wide analysis of HDAC function. *Trends Genet.* **21**, 608–615

31. Carmen, A. A., Griffin, P. R., Calaycay, J. R., Rundlett, S. E., Suka, Y., and Grunstein, M. (1999) Yeast HOS3 forms a novel trichostatin A-insensitive homodimer with intrinsic histone deacetylase activity. *Proc. Natl. Acad. Sci. U. S. A.* **96**, 12356–12361

32. Rundlett, S. E., Carmen, A. A., Kobayashi, R., Bavykin, S., Turner, B. M., and Grunstein, M. (1996) HDA1 and RPD3 are members of distinct yeast histone deacetylase complexes that regulate silencing and transcription. *Proc. Natl. Acad. Sci. U. S. A.* **93**, 14503–14508

33. Ahn, S. H., Diaz, R. L., Grunstein, M., and Allis, C. D. (2006) Histone H2B deacetylation at lysine 11 is required for yeast apoptosis induced by phosphorylation of H2B at serine 10. *Mol. Cell* **24**, 211–220

34. Wang, M., and Collins, R. N. (2014) A lysine deacetylase Hos3 is targeted to the bud neck and involved in the spindle position checkpoint. *Mol. Biol. Cell* **25**, 2720–2734

35. Kumar, A., Sharma, P., Gomar-Alba, M., Shcheprova, Z., Daulny, A., Sanmartín, T., *et al.* (2018) Daughter-cell-specific modulation of nuclear pore complexes controls cell cycle entry during asymmetric division. *Nat. Cell Biol.* **20**, 432–442

36. Dong, J., Ning, W., Liu, W., and Bruening, M. L. (2017) Limited proteolysis in porous membrane reactors containing immobilized trypsin. *Analyst* **142**, 2578–2586

37. Leng, K. R. W., Castañeda, C. A., Decroos, C., Islam, B., Haider, S. M., Christianson, D. W., *et al.* (2019) Phosphorylation of histone deacetylase 8: structural and mechanical analysis of the phosphomimetic S39E mutant. *Biochemistry* **58**, 4480–4493

38. Moore, D. (2016) Panobinostat (Farydak): a novel option for the treatment of relapsed or relapsed and refractory multiple myeloma. *P T* **41**, 296–300

39. Gintjee, T. J., Donnelley, M. A., and Thompson, G. R., 3rd (2020) Aspiring antifungals: review of current antifungal pipeline developments. *J. Fungi (Basel)* **6**, 28

40. Otwinowski, Z., and Minor, W. (1997) Processing of X-ray diffraction data collected in oscillation mode. *Methods Enzymol* **276**, 307–326

41. Adams, P. D., Afonine, P. V., Bunkóczi, G., Chen, V. B., Davis, I. W., Echols, N., *et al.* (2010) Phenix: a comprehensive Python-based system for macromolecular structure solution. *Acta Crystallogr. D Biol. Crystallogr.* **66**, 213–221

42. Emsley, P., and Cowtan, K. (2004) Coot: model-building tools for molecular graphics. *Acta Crystallogr. D Biol. Crystallogr.* **60**, 2126–2132

43. Hai, Y., and Christianson, D. W. (2016) Histone deacetylase 6 structure and molecular basis of catalysis and inhibition. *Nat. Chem. Biol.* **12**, 741–747

44. Waterhouse, A., Bertoni, M., Bienert, S., Studer, G., Tauriello, G., Gumienny, R., *et al.* (2018) SWISS-MODEL: homology modelling of protein structures and complexes. *Nucleic Acids Res.* **46**, W296–W303

45. Anandakrishnan, R., Aguilar, B., and Onufriev, A. V. (2012) H++ 3.0: automating pK prediction and the preparation of biomolecular structures for atomistic molecular modeling and simulations. *Nucleic Acids Res.* **40**, W537–W541

46. Maier, J. A., Martinez, C., Kasavajhala, K., Wickstrom, L., Hauser, K. E., and Simmerling, C. (2015) ff14SB: improving the accuracy of protein side chain and backbone parameters from ff99SB. *J. Chem. Theory Comput.* **11**, 3696–3713

47. Zhengwei, P., Ewig, C. S., Hwang, M. J., Waldman, M., and Hagler, A. T. (1997) Comparison of simple potential functions for simulating liquid water. *J. Phys. Chem. A* **101**, 7243–7252

48. Case, D. A., Ben-Shalom, I. Y., Brozell, S. R., Betz, R. M., Cai, Q., Cerutti, D. S., *et al.* (2018) *Amber 18*, University of California, San Francisco, CA

49. Ryckaert, J. P., Ciccotti, G., and Berendsen, H. (1977) Numerical integration of the Cartesian equations of motion of a system with constraints: molecular dynamics of n-alkanes. *J. Comput. Phys.* **23**, 327–341

50. Darden, T. A., York, D. M., and Pedersen, L. G. (1993) Particle mesh Ewald - an N.log(N) method for Ewald sums in large systems. *J. Comput. Chem.* **18**, 1463–1472

51. Morris, G. M., Huey, R., Lindstrom, W., Sanner, M. F., Belew, R. K., Goodsell, D. S., *et al.* (2009) AutoDock4 and AutoDockTools4: automated docking with selective receptor flexibility. *J. Comput. Chem.* **30**, 2785–2791

52. Sterling, T., and Irwin, J. J. (2015) ZINC 15–ligand discovery for everyone. *J. Chem. Inf. Model.* **55**, 2324–2337